Carbon 122 (2017) 451–461

Contents lists available at ScienceDirect

Carbon

journal homepage: www.elsevier.com/locate/carbon

Tomography-based radiative characterisation of decomposing carbonaceous heat shield materials

Nikhil Banerji [a, b], Pénélope Leyland [b], Sophia Haussener [a, *]

[a] Laboratory of Renewable Energy Science and Engineering, Station 9, Ecole Polytechnique Fédérale de Lausanne, 1015, Switzerland
[b] Interdisciplinary Aerodynamics Group, Station 9, Ecole Polytechnique Fédérale de Lausanne, 1015, Switzerland

ARTICLE INFO

Article history:
Received 13 April 2017
Received in revised form
16 June 2017
Accepted 17 June 2017
Available online 20 June 2017

ABSTRACT

This work evaluates the changes in radiative properties of two decomposing carbonaceous porous materials, each composed of two semi-transparent, homogeneous and isotropic phases. The understanding of the complex dependence of macroscopic optical behaviour on material microstructure, bulk phase properties and the wavelength of incoming radiation is paramount for modelling, design and optimisation of systems incorporating such media. Experimental and numerical techniques were combined to solve the homogenised radiative transfer equations using Monte Carlo ray tracing in the limit of geometrical optics. Effective radiative properties required by these equations were determined by Monte Carlo techniques using the exact 3D microstructures of the samples, obtained through high-resolution synchrotron computed tomography. This methodology is applied to a medium density carbon phenolic and a high density graphite reinforced polymer composite, each composed of semi-transparent solid and fluid phases. The extent of material decomposition is seen to affect the absorption behaviour of both samples. This effect is more obvious in the lower density carbon phenolic, where an 18% increase in absorptance is observed due to decomposition, compared to an increase of just 2% for the graphite. A library of absorption data is presented for use in continuum heat transfer modelling of similar chemically reacting macroporous carbon composites.

1. Introduction

Spacecraft employ composite materials as Thermal Protection Systems (TPS) to survive entering a planetary atmosphere at hypersonic speeds. Under intense convective and radiative heating from the surrounding shock layer, these composites decompose and erode, transferring heat away from the payload. Lower density TPS employing porous carbon phenolics have been considered in an attempt to reduce structural and fuel load and increase payload capacity.

Post-flight evaluation of the Stardust capsules forebody heat shield [1] as well as statistical modelling of TPS material microstructure [2] have recently confirmed the volumetric nature of ablation. In-depth oxidation leaves the carbon preform exposed to its extreme operating environment, where radiation becomes a significant (and eventually, dominant) mode of heat transfer [3]. The majority of the heavy carbonaceous molecules released during the break-down of the resin demonstrate semi-transparent behaviour and can significantly alter the radiative properties of the TPS. In order to evaluate the flight worthiness of these modern lightweight composites, it is imperative to fully understand their response to extreme conditions.

Radiation within fibrous insulators has previously been accounted for in simplified or artificial porous geometries through the use of semi-analytical models [4–7] or by applying radiative transfer equations (RTEs) with appropriate apparent properties [8–10]. Recent advances in computational techniques allow for the incorporation of the exact morphology from 3D data obtained by imaging techniques such as computed tomography [11–13]. These investigations rely on volume averaging theory for the derivation of the homogenised RTEs [14–16]. The incorporated effective radiative properties can be obtained by using Monte Carlo methods, in the limit of geometrical optics [8]. The theory has been derived for multi-component media with semi-transparent homogeneous, isotropic single phases [14].

To date computational applications have assumed two phases, either transparent and opaque [14], or transparent and semi-

* Corresponding author.
E-mail address: sophia.haussener@epfl.ch (S. Haussener).

http://dx.doi.org/10.1016/j.carbon.2017.06.045
0008-6223/

Nomenclature

A	Absorptance
d	Diameter or characteristic length, m
f_v	Phase volume fraction
I_i	Volume averaged radiative intensity in phase i, $Wm^{-3}\ sr^{-1}$
k	Imaginary part of complex refractive index
n	Real part of complex refractive index
R	Reflectance
Tr	Transmittance
x	Size parameter
$\widehat{\mathbf{s}}$	Unit direcitonal vector
$\mathbf{x}$	Position vector

Greek symbols

β	Extinction coefficient, m^{-1}
Γ	Resin volume fraction
Ω	Solid angle, sr
ω	Scattering albedo
Φ	Scattering phase function, sr^{-1}
ϕ	Porosity
ρ_i	Density of component phase, kg m^{-3}
ρ_r	Directional-hemispherical reflectivity
σ_s	Scattering coefficient, m^{-1}
λ	Wavelength, m

Subscripts

i,j	Phase declarations
b	Blackbody
d	Discrete scale
refl	Reflection
refr	Refraction
REV	Representative elementary volume

transparent [16–18]. In a variety of applications however, there is a possibility of both phases being semi-transparent in the wavelength range of interest, or, for reacting media, during part of the reaction process [19]. The resulting macroscopic optical behaviour is dependent on the material microstructure, bulk properties of the phases and inter-phase characteristics. Incorporating this macroscopic optical behaviour into a coupled multi-physics computation or investigation requires detailed knowledge of the effect of the different phases and their properties on the overall optical behaviour.

This work aims to quantify the influence of the semi-transparent bulk phases on the macroscopic optical behaviour of a sample and to provide correlations based on single phase bulk material properties. These correlations are readily incorporated into macroscopic simulations. The effective properties, calculated by applying the discrete-scale approach to the real 3D geometries of the samples obtained by computed tomography, are used to derive continuum radiative properties for a semi-infinite slab of the material sample. The two-phase media considered are a medium density carbon phenolic ablator [20] and a high density graphite reinforced polymer ablator [21], each comprised of semi-transparent fluid and solid phases.

2. Methodology

This study considers quasi-steady radiative transfer in a medium consisting of two semi-transparent phases. The phase compositions are dependent on the extent of reaction (i.e. decomposition): (i) initially the sample consists of solid fibres bound by thermoset resin and an air filled gas phase, and (ii) after the heterogeneous reactions, the solid phase comprises solely of the fibres and the gas phase contains a mixture of strongly attenuating pyrolysis gases and air. The equations for the assessment of radiative transfer, given in the next section, are solved using Monte Carlo ray tracing. The method is subject to the following assumptions: (i) both phases are homogeneous and isotropic; (ii) each phase has constant, non-polarising optical properties; (iii) both phases are at local thermodynamic equilibrium; (iv) the characteristic length of each component is greater than the wavelengths of interest, validating the application of geometrical optics; (v) negligible diffraction; (vi) all components are at rest as compared to the speed of light and (vii) dependent-scattering effects are negligible. The main governing equations, derived by Lipiński et al. [14], are summarised in Section 2.1.

2.1. Governing equations and implementation

The quasi-steady homogenised RTEs for a multi-phase medium comprising of two semi-transparent phases are given by Equation (1), where the spectral subscript has been omitted for brevity. This set of equations is derived from the discrete-scale RTEs valid in the individual phases and the corresponding inter-phase boundary conditions [14]. I_i is the volume-averaged local intensity, $I_{b,i}$ is the volume-averaged blackbody intensity in vacuum, κ_i, $\sigma_{s,ij}$, $\Phi_{i,j}$ are the effective absorption and scattering coefficients and the scattering phase functions respectively.

$$\begin{aligned}\widehat{\mathbf{s}}\cdot\nabla I_i\left(\mathbf{x},\widehat{\mathbf{s}}\right) = &-\beta_i I_i\left(\mathbf{x},\widehat{\mathbf{s}}\right)+\kappa_{d,i}I_{b,i}\left(\mathbf{x},\widehat{\mathbf{s}}\right)\\ &+\frac{\sigma_{s,ii}}{4\pi}\int_{\Omega_{i=0}}^{4\pi} I_i(\mathbf{x},\widehat{\mathbf{s}}_i)\Phi_{ii}\left(\widehat{\mathbf{s}}_i,\widehat{\mathbf{s}}\right)d\Omega_i\\ &+\frac{\sigma_{s,ji}}{4\pi}\int_{\Omega_{i=0}}^{4\pi} I_j(\mathbf{x},\widehat{\mathbf{s}}_i)\Phi_{ji}\left(\widehat{\mathbf{s}}_i,\widehat{\mathbf{s}}\right)d\Omega_i,\\ &i,j=1,2;i\neq j\end{aligned} \tag{1}$$

The effective properties, given in Equations (2)–(6), are a combination of single phase bulk material properties ($\beta_{d,i}$, $\kappa_{d,i}$, $\sigma_{d,s,i}$, $\Phi_{d,ij}$) and morphology-dependent properties ($\sigma_{refl,s,i}$ and $\sigma_{refr,s,i}$),

$$\sigma_{s,ii}=\sigma_{s,refl,i}+\sigma_{s,d,i} \tag{2}$$

$$\sigma_{s,ij}=\sigma_{s,refr,i} \tag{3}$$

$$\Phi_{ii}=\sigma_{s,ii}^{-1}\left(\Phi_{refl,i}\sigma_{s,refl,i}+\Phi_{d,i}\sigma_{s,d,i}\right) \tag{4}$$

$$\Phi_{ij}=\sigma_{s,ij}^{-1}\Phi_{refr,i}\sigma_{s,refr,i} \tag{5}$$

$$\beta_i=\beta_{d,i}+\sigma_{s,refl,i}+\sigma_{s,refr,i} \tag{6}$$

Simulations are conducted for 10 mm thick semi-infinite slabs, exposed to a diffuse beam parallel to the surface normal and a perfectly black boundary at the rear. Reflectance, R, is the integrated flux leaving the inlet surface and absorptance, $A = 1 - R - Tr$,

where *Tr* is the slab transmittance, i.e. the integrated flux leaving the outlet surface. The two-phase morphology associated properties are determined by direct pore-level simulations [8,11,22] applied to the real 3D geometries of the samples obtained by high resolution synchrotron computed tomography.

2.2. Composite sample morphology

To evaluate the feasibility of using the tomography-based approach for TPS materials, preliminary discrete-scale morphological and radiative characterisation of a highly porous alumina foam has been conducted, using low resolution, low flux tomography [23]. This investigation revealed several insufficiencies in the data quality, contrast and resolution, leading to difficulty in image segmentation. Higher beam energies and higher resolution were obtained via a campaign, conducted at the TOMCAT beamline of the Swiss Light Source (SLS) at the Paul Scherrer Institute [24]. The data were collected using an 18 keV photon energy, an exposure time of 130 ms, and a microscope allowing for a spatial resolution of 0.33 μm resulting in a field of view of 2560 × 2560 x 2160 pixels (845 × 845 × 713 μm^3). In composite materials, the resin phase typically presents nanometre sized structural characteristics. It is therefore likely that the 0.33 μm pixel size is not sufficient to resolve these structures. The chosen segmentation is therefore an approximation of the gas-resin phase morphology, within the limits of the resolution of the imaging technique.

To examine the effect of material decomposition, the gas phase, occupying the pore space, is artificially adapted via image segmentation to (i) include only the air phase (virgin case) and to (ii) include air and resin phases where the resin phase is assumed decomposed and comprises of highly attenuating pyrolysis gases (decomposed case). In both cases, one phase combines two separate components along with their bulk properties. This approximation avoids the use of a three-phase model. This is shown in 3D surface renderings of the carbon phenolic and graphite samples in Fig. 1a and 1b respectively. The front half each image portrays the material in its decomposed state, where complete gassification of the resin leaves a solid phase enveloped in attenuating gases. The back halves of the samples portray the virgin state, where the solid phase is made up of the fibres and thermoset resin. Fig. 1a and 1b are for illustrative purposes only. For all simulations, samples are considered either fully decomposed or virgin and do not possess a moving reaction front. The indices 1 and 2 are used for the gas and solid phase respectively.

The investigated samples show structural anisotropy. In order to reduce the complexity of results, which would have to be reported as a function of polar and azimuthal angles, direction-averaged properties were calculated.

Table 1
Numerically determined porosity, density, mean solid and pore diameters, REV edge length and size parameters calculated for a reference wavelength of 1 μm, for the four samples investigated.

	Carbon Phenolic		Graphite	
	Virgin	Decomposed	Virgin	Decomposed
Porosity	0.57	0.81	0.08	0.28
Density (kg m^{-3})	602	266	1435	1123
d_{pore} (μm)	11	20	8	10
d_{solid} (μm)	15	11	25	22
l_{REV} (mm)	0.11	0.17	0.16	0.15
Ref. size parameter, x_{ref}	35.78	62.49	23.84	30.07

3. Results

3.1. Morphological characterisation

Porosities are calculated by two-point correlations using a Monte Carlo method [25]. The porosity is seen to increase with decomposition (as expected due to resin outgassing) from 0.57 to 0.81 for the carbon phenolic and from 0.08 to 0.28 for the graphite sample. It is possible to evaluate the bulk material density of each sample via Equation (7), commonly used in literature to model charring ablators [26].

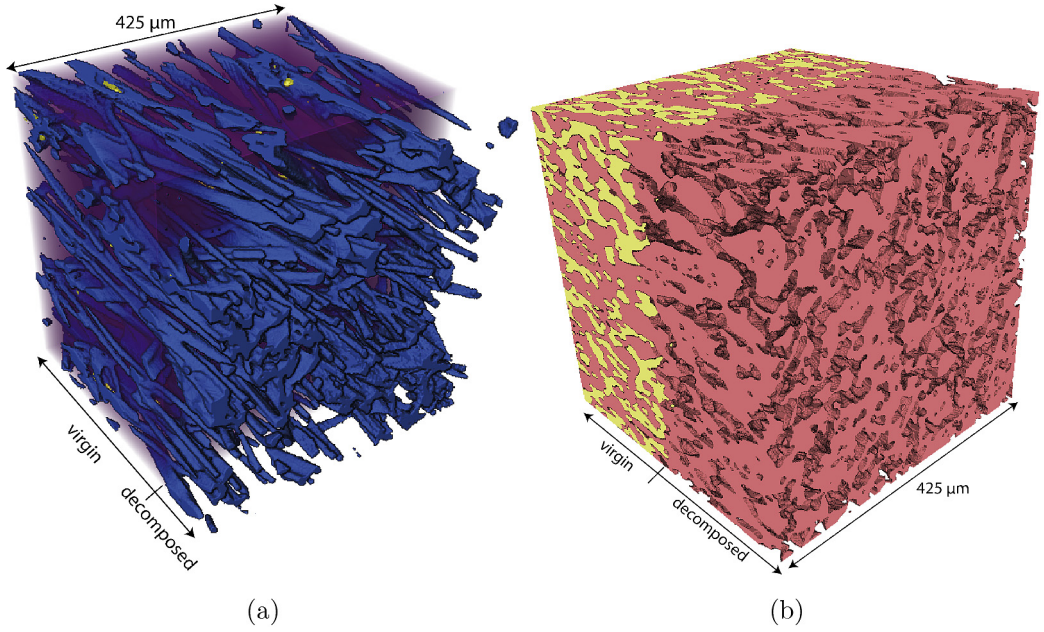

Fig. 1. 3D renderings of the sample geometries for (a) the medium porosity carbon phenolic composite sample (solid fibre phase in blue, resin phase in purple and air in yellow) and (b) the high density graphite reinforced polymer composite sample (solid phase in pink, resin phase in yellow and air is not visible due to low volume fraction). The back of the sample is in its virgin state and the front in the decomposed state. (A colour version of this figure can be viewed online.)

$$\rho_{bulk} = (1-\phi)[\Gamma(\rho_A + \rho_B) + (1-\Gamma)\rho_C] \quad (7)$$

As an input to this equation, the resin phase is assumed to comprise of a combination of two polymers, with densities, $\rho_A = 300$ kg·m^{-3} and $\rho_B = 900$ kg·m^{-3} [27,28]. The carbon fibre matrix has a density, $\rho_C = 1600$ kg·m^{-3} and Γ is the resin volume fraction and is said to equal to 0.5 and 0.1 for the carbon phenolic and graphite reinforced polymer composites respectively [27,28]. By applying the porosities calculated based on the tomography data, it is possible to evaluate bulk densities (Table 1) for comparison with estimations given in literature [20,21]. The calculated values fall within the range of densities given by the manufacturers, within the limits of uncertainty.

The normalised pore-size distribution based on mathematical opening distributions with spherical structuring elements [29] is presented in Fig. 2a. With all its resin reacted, the decomposed carbon phenolic sample shows the largest pores. Pore sizes increase very slightly with decomposition for the graphite sample. The mean pore size of the virgin samples are 11 and 8 μm for the carbon phenolic and graphite samples respectively. For the decomposed samples d_{pore} are 20 and 10 μm respectively. Fig. 2b shows the normalised solid phase distributions with a mean solid phase diameter, d_{solid}, of 15 μm and 11 μm for the virgin and decomposed carbon phenolic respectively. For the virgin and decomposed graphite, d_{solid} is 25 μm and 22 μm respectively.

The representative elementary volume edge length (l_{REV}), describing the smallest volume for which continuum can be assumed, is estimated based on porosity calculations on subsequently growing sample sub-volumes and is assumed sufficient when the solutions converge to the porosity within a band of ±0.025. The edge length of a cubic REV, l_{REV}, for the four samples investigated are 0.11 mm, 0.17 mm, 0.16 mm and 0.15 mm respectively. For the discrete-scale calculations, a cubic sample of 0.27 mm edge length was used to ensure a constant domain size for all samples investigated, which lies well within the required REV size. All morphological characteristics and the reference size parameter, used if not otherwise indicated, are summarised in Table 1. The reference size parameter ($x_{ref} = \pi d_{pore}/\lambda$) is based on the calculated mean pore diameter for a wavelength of 1 μm.

3.2. Effective radiative properties

Calculations of the effective radiative properties are performed for a combination of bulk properties at size parameters between 5 and 500, corresponding to wavelengths between 0.041 μm and 16.39 μm. Reflection and refraction are modelled by Fresnel's equations and the generalised form of Snell's law [30] at the specularly reflecting interfaces. Both phases are assumed to be semi-transparent, i.e. its bulk absorption and scattering coefficients, $\kappa_{d,i}$, $\sigma_{d,s,i}$ are equal to a non-zero value and its refractive indices do not equal 1. For cases such as the virgin graphite, where smallest pore diameters are on the order of the wavelength studied, wave effects estimated via Mie theory suggest values approximately 11% greater compared to those calculated using the current methodology based on geometrical optics. The assumption of independent scattering is confirmed using the criteria by Tien et al. [31] for the smallest observed size parameter, $x = 5$ and a pore volume fraction of $f_v = 0.08$.

3.2.1. Extinction coefficient

The product of mean pore diameter and effective extinction coefficient, β_1, of the air or reactive gas-filled pore phase for all four samples is plotted against the normalised bulk extinction coefficient, $\beta_1 d_{pore}$, of the same phase and shown in Fig. 3a. The behaviour can be divided into two separate responses. For low normalised bulk extinction coefficients ($\beta_1 d_{pore} < 0.01$), little attenuation in the gas phase is observed and the morphological effects dominate. The numerical value of β_1 in the limit of small $\beta_{d,1}$ depends only on the morphological properties of the samples. The simplest morphological characteristic, the porosity, shows a clear trend: the effective extinction coefficient is inversely proportional to sample porosity. The decomposed carbon phenolic, with the highest porosity, has the lowest effective extinction coefficient, β_1. The higher density virgin and decomposed graphite samples show significantly more extinction in the morphologically dominated response.

Once $\beta_1 d_{pore}$ increases past a threshold ($\sim 10^{-1}$ for both the carbon phenolic and graphite), internal radiation starts to contribute heavily to the effective properties in a directly

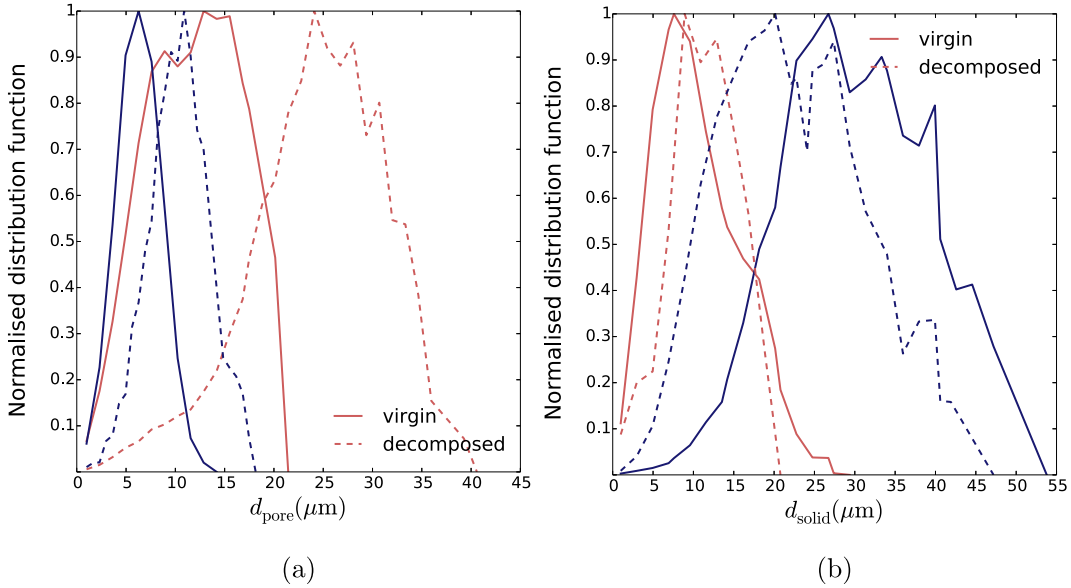

Fig. 2. Morphological opening size distributions for the virgin (solid line) and decomposed (dashed line) forms of the carbon phenolic (blue) and graphite reinforced polymer (red) samples for (a) the gas phase, and (b) the solid phase. (A colour version of this figure can be viewed online.)

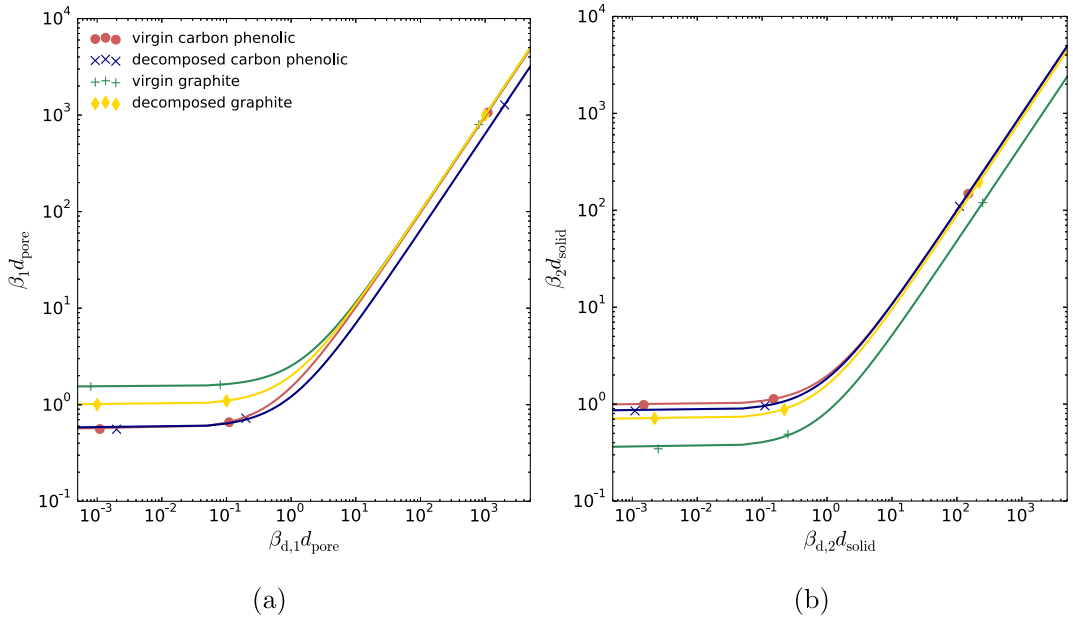

Fig. 3. Normalised effective extinction coefficient, $\beta_i d_i$, as a function of normalised bulk extinction coefficient of the (a) gas ($\beta_{\text{d},1} d_{\text{pore}}$), and (b) solid ($\beta_{\text{d},2} d_{\text{solid}}$) phases. The lines indicate the fits detailed in Table 2. (A colour version of this figure can be viewed online.)

Table 2
Dependence of the effective extinction coefficient of the gas and solid phase on the discrete-scale extinction coefficient of the gas and solid phase, respectively. The functions have been obtained by fitting the calculated data points, indicated in Fig. 3.

		Carbon Phenolic		Graphite	
		Virgin	Decomposed	Virgin	Decomposed
$\beta_1 d_{\text{pore}}$	$\beta_{\text{d},1} d_{\text{pore}} < 10^{-1}$	$0.48\beta_{\text{d},1} d_{\text{pore}} + 531.79$	$0.32\beta_{\text{d},1} d_{\text{pore}} + 0.33$	$0.51\beta_{\text{d},1} d_{\text{pore}} + 407.41$	$0.51\beta_{\text{d},1} d_{\text{pore}} + 509.26$
	$\beta_{\text{d},1} d_{\text{pore}} > 10^{-1}$	$2.99\beta_{\text{d},1} d_{\text{pore}} + 0.33$	$1.81\beta_{\text{d},1} d_{\text{pore}} + 0.36$	$129.11\beta_{\text{d},1} d_{\text{pore}} + 10.33$	$129.11\beta_{\text{d},1} d_{\text{pore}} + 12.91$
$\beta_2 d_{\text{solid}}$	$\beta_{\text{d},2} d_{\text{solid}} < 10^{-1}$	$327.31\beta_{\text{d},2} d_{\text{solid}} + 0.49$	$387.15\beta_{\text{d},2} d_{\text{solid}} + 0.43$	$69.17\beta_{\text{d},2} d_{\text{solid}} + 0.17$	$161.75\beta_{\text{d},2} d_{\text{solid}} + 0.36$
	$\beta_{\text{d},2} d_{\text{solid}} > 10^{-1}$	$3.77\beta_{\text{d},2} d_{\text{solid}} + 0.56$	$4.37\beta_{\text{d},2} d_{\text{solid}} + 0.48$	$0.98\beta_{\text{d},2} d_{\text{solid}} + 0.24$	$1.99\beta_{\text{d},2} d_{\text{solid}} + 0.44$

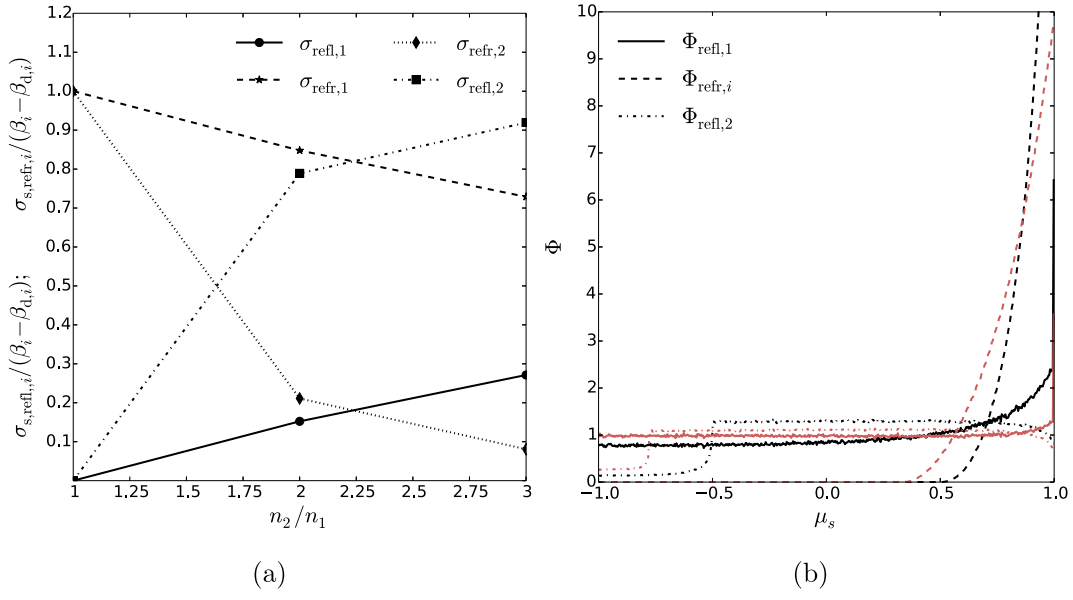

Fig. 4. (a) Effective normalised scattering coefficients as a function of refractive index ratio (n_2/n_1) for virgin carbon phenolic. (b) Effective scattering phase function for scattering between different phases (phase 1: gas, phase 2: solid) for $n_2/n_1 = 2$ (red lines) and $n_2/n_1 = 3$ (black lines). (A colour version of this figure can be viewed online.)

Table 3
Coefficients of the seventh order polynomial fit to the scattering phase functions $\Phi_{\text{refl},1}$, $\Phi_{\text{refr},i}$ and $\Phi_{\text{refl},2}$ for all four sample morphologies and the respective root-mean-square error (RMSE).

n_2/n_1	$f(\mu)$	a_0	a_1	a_2	a_3	a_4	a_5	a_6	a_7	RMSE
3	$\Phi_{\text{refl},1}$	0.8311	0.8164	−0.5952	−0.4015	0.4374	0.3561	0.1639	0.8369	0.025
	$\Phi_{\text{refr},i}$	11.95	14.80	−4.116	−7.353	0.9844	1.167	−0.1128	−0.0334	0.071
	$\Phi_{\text{refl},2}$ ($\mu_s > -0.496$)	−5.31	6.666	0.3121	−2.498	0.2017	0.2053	0.0092	1.291	0.016
	$\Phi_{\text{refl},2}$ ($\mu_s < -0.496$)	37985.85	204757.75	469654.75	594114.19	447589.81	200803.33	49671.38	5226.6	0.029
2	$\Phi_{\text{refl},1}$	0.3989	0.3937	−0.3803	−0.3207	0.1614	0.0784	−0.0301	0.9771	0.019
	$\Phi_{\text{refr},i}$	−1.438	−1.724	3.993	7.127	2.634	−0.5232	−0.2954	−0.0047	0.036
	$\Phi_{\text{refl},2}$ ($\mu_s > -0.771$)	−1.363	0.1673	1.428	−0.1281	−0.4855	−0.0166	0.0559	1.111	0.014
	$\Phi_{\text{refl},2}$ ($\mu_s < -0.771$)	8.42	5.29e7	1.42e8	2.13e8	1.90e8	1.02e8	3.04e7	3.88e6	0.024

proportional manner, leading to an increased slope in the linear rise of β_1 with respect to $\beta_{d,1}$. Similar behaviour can be seen for β_2, shown in Fig. 3. However, in this case, the volume fraction of the solid phase is the relevant characteristic morphological property, with decreasing effective extinction coefficient for an increase in solid volume fraction.

A set of semi-empirical linear curve fitting functions for the data presented in Fig. 3, is presented in Table 2. The curve fits can be used to estimate effective extinction coefficients of similar material samples and their corresponding changes with respect to reaction extent or wavelength (via changes in size parameter) by moving along the respective curve in Fig. 3. These values hold true for any combination of wavelength and bulk material properties, both of which affect the bulk extinction coefficient.

3.2.2. Scattering

The normalised scattering coefficients $\sigma_{\text{refl},s,i}$ and $\sigma_{\text{refr},s,i}$, are shown in Fig. 4a, as a function of the refractive index ratio (n_2/n_1) for the virgin carbon phenolic sample at $n_2 = 1, 2, 3$ and $n_1 = 1$. With increasing refractive index ratio, the radiation scattered within a single phase ($\sigma_{\text{refl},s,i}$) increases and the radiation scattered from one phase to another ($\sigma_{\text{refr},s,i}$) decreases due to a combination of total internal reflection and increased directional hemispherical reflectivity of the interface. Morphology does not significantly affect the scattering coefficients as the decomposed sample exhibits identical behaviour as do both graphite samples. This is consistent with previous observations of the insensitivity of the scattering behaviour on the sample morphology [22]. No wavelength dependence is observed for the normalised scattering coefficients assuming the real part of the refractive index at a particular wavelength is given by the ratio indicated.

The scattering phase function is presented in Fig. 4b, as a function of the directional cosine of the scattering angle, $\mu_s = \cos(\theta)$. The assumption of perfectly reversible interface behaviour for photons scattered at the outer or inner boundary produces identical inter-phase scattering functions ($\Phi_{\text{refr},1} = \Phi_{\text{refr},2}$).

$\Phi_{\text{refr},i}$ show a peak in the forward direction, which becomes more pronounced with increasing ratio of refractive indices due to increased directional hemispherical reflectivity of the interface at a majority of incidence angles for $n_2/n_1 = 3$. The phase function, $\Phi_{\text{refr},i}$ drops to zero in the backward direction as total reflection limits the accessibility of angles below $\mu_s < -\sqrt{1-\mu^2_{\text{refl,tot}}}$. Scattering due to reflection at the interface of the gas phase ($\Phi_{\text{refl},1}$) has access to all scattering angles and the scattering behaviour is generally isotropic, with a small peak in the forward direction. For the solid phase ($\Phi_{\text{refl},2}$), the phase function is flat in the forward direction, and rapidly approaches zero in the backward direction due to total internal reflection limiting angles below $\mu_s < 1 - 2\mu^2_{\text{refl,tot}}$ [22]. The forward scattering, highly anisotropic behaviour for $\Phi_{\text{refl},2}$ is consistent with the work of Lee [6] for fibrous insulations. The curves shown in Fig. 4b are for the virgin carbon phenolic sample. However, no sensitivity of the effective scattering phase functions with respect to morphological differences or size parameter were observed and consequently these functions are valid for both samples in their virgin and decomposed states. Coefficients of the seventh order polynomial fit to the scattering phase functions are detailed in Table 3.

Along with the effective extinction coefficients calculated above, this scattering data can be supplied to the continuum-scale RTEs to accurately describe radiative heat exchange in two-phase media with known bulk material properties and of similar porosity to the samples considered in this paper. The RTEs can then be coupled to the energy equation and support the accurate solution of heat and mass transfer characteristics in complex macroporous reacting media.

3.3. Macroscopic optical properties

3.3.1. General solution

The dependency of absorptance on bulk extinction coefficient for each of the four investigated samples is shown in Fig. 5, with $n_2/n_1 = 2$, $\sigma_{s,d,i} = 0$ and a wavelength of 1 μm (i.e. x_{ref}). For $\beta_{d,1}\lambda \leq 10^{-1}$ (Fig. 5b, 5c and 5d) and $\beta_{d,2}/\beta_{d,1} < 10^{-2}$, the decomposed carbon phenolic sample, which has the highest porosity of the four, shows the strongest absorptance and the high density virgin graphite sample shows the lowest absorptance. In this range the gas phase is dominating the absorption behaviour. The smaller $\beta_{d,1}$, the smaller this asymptotic absorption value. For increasing $\beta_{d,2}/\beta_{d,1}$ ratios, the solid phase starts to also contribute to absorption, increasing the absorptivity. For cases with low gas phase bulk absorption ($\beta_{d,1}\lambda < 10^{-2}$) as shown in Fig. 5c and 5d, the contribution of the solid phase becomes so significant that the absorptivity of the low porosity and high porosity sample cases cross and the virgin graphite sample, which has the lowest porosity of the four, shows the highest absorptance and the decomposed carbon phenolic sample shows the smallest absorptance.

This crossover is not visible for the cases with very large $\beta_{d,1}$ (Fig. 5a and 5b), as with increasing $\beta_{d,2}/\beta_{d,1}$, k_2 grows, and if $k_2 > 1$, direct reflection by the solid phase at the inlet boundary starts to dominate the radiation behaviour. In this case (i.e. $\beta_{d,1}\lambda \geq 10^{-2}$ and for large $\beta_{d,2}/\beta_{d,1}$), the low porosity sample has the largest fraction of direct reflection and consequently the lowest absorptance. The dominance of the inlet face is also visible for the cases with lower $\beta_{d,1}$ leading to a decrease in calculated absorptance with increasing $\beta_{d,2}/\beta_{d,1}$ and eventually another cross of the low and high porosity cases and a drop in the absorptance for all cases.

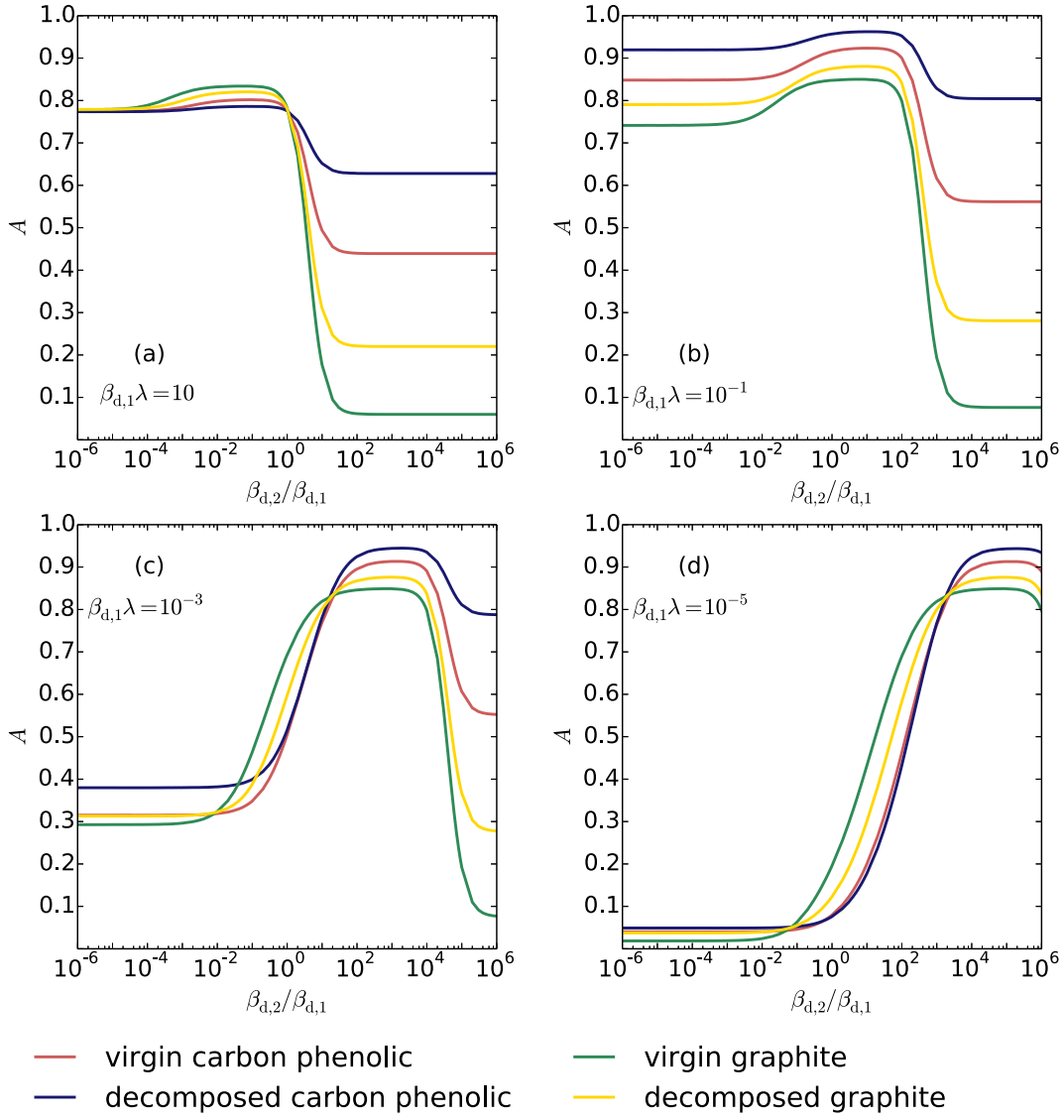

Fig. 5. Absorptance of a 10 mm thick slab exposed to diffuse irradiation at a wavelength of 1 μm (i.e. x_{ref}) composed of the four samples for varying bulk extinction coefficients, $n_2/n_1 = 2$ and for $\sigma_{s,d,i} = 0$. (A colour version of this figure can be viewed online.)

For $\beta_{d,1}\lambda \geq 10^{-1}$ and low $\beta_{d,2}/\beta_{d,1}$, shown in Fig. 5a and 5b, direct reflection at the inlet boundary is observed, but this time due to the gas phase where $k_1 > 1$. Absorptance is therefore inversely proportional to porosity, with the high porosity decomposed carbon phenolic displaying low absorptance. Highest absorptance is seen in the virgin graphite sample due to its low gas phase volume fraction.

For cases where $\beta_{d,1}\lambda \geq 10^{-5}$, slab transmittance is always zero for all investigated samples due to large sample thickness coupled with the presence of highly attenuating bulk phases. Everything that is not absorbed, is therefore reflected. However, for $\beta_{d,1}\lambda \leq 10^{-5}$, the virgin and decomposed graphite samples show up to 9% and 3% transmittance respectively, for the small values of $\beta_{d,2}/\beta_{d,1} < 1$, as shown in Fig. 6. Due to the low volume fraction of the attenuating gas phase in both virgin and decomposed graphite, as well as extremely low solid phase bulk extinction coefficients, radiation is transmitted across the slab. The same phenomenon is insignificant ($Tr < 0.005$) for the carbon phenolic samples due to the increased presence of the gas phase.

3.3.2. Application to thermal protection systems

The data in Fig. 5 is usable for any two-phase medium with a porosity similar to the carbon phenolic or graphite samples. Here, the absorptance of a 10 mm thick slab of the investigated TPS materials is calculated. Lee [7] computed the bulk extinction coefficient for a carbon fibre matrix as 9000 m^{-1} while White [32] calculated the same from experimental measurements to be 7700 m^{-1} for a PICA material sample. Using a plasma radiation database, PARADE v3.2 [33], gas phase absorption coefficients are calculated for an equilibrium mixture of pyrolysis products (given in Table 4) at 3000 K (decomposed case). In a wavelength range of 50–5500 nm, the spectrally averaged gas phase bulk absorption coefficient was estimated to be 10^5 m^{-1}. For the virgin samples, gas phase absorption coefficient is assumed to be 10 m^{-1}, as this is the lowest value investigated. Using Lee's estimation of the bulk extinction coefficient for the solid phase, $\beta_{d,2}/\beta_{d,1} \sim 900$ for the virgin case and $\beta_{d,2}/\beta_{d,1} \sim 0.09$ for the decomposed case.

From Fig. 5b and 5d, assuming incoming radiation at a wavelength of 1 μm, an increase in the absorption during decomposition of the carbon phenolic from 0.76 to 0.94 is observed. The

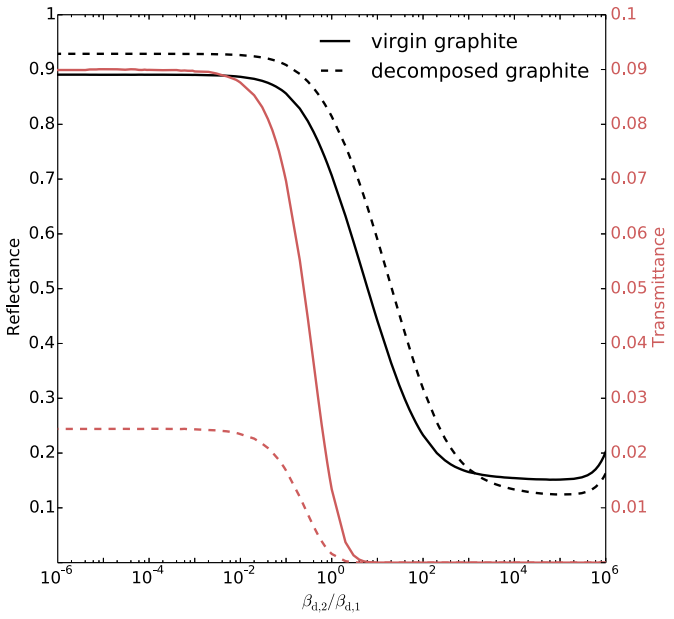

Fig. 6. Fraction of incoming radiation, at a wavelength of 1 μm, that is reflected and transmitted by the virgin and decomposed graphite samples for $\beta_{d,1} = 10$ m^{-1}, $n_2/n_1 = 2$ and $\sigma_{s,d,i} = 0$. (A colour version of this figure can be viewed online.)

reflectance decreases from 0.24 to 0.06. Using the same ratios of bulk coefficients - on the assumption that the carbon fibre matrix would be similar, and any hydrocarbon based resin would decompose to form the same products at high temperatures - absorptance in pyrolysing graphite increases from 0.82 to 0.84, while reflectance decreases from 0.18 to 0.14. Radiation is not transmitted across either sample for all extents of decomposition. The change in macroscopic optical properties is more critical for the lower density carbon phenolic, compared to the higher density graphite. These findings are significant, especially given the desire to replace current TPS materials with ones of low to medium density.

3.3.3. Spectral dependence

The spectral dependence of absorptance for the four samples under consideration is presented in Fig. 7a, via evaluation at different size parameters $5 < x < 500$, with $n_2/n_1 = 2$, $k_2/k_1 = 0.01$ for $k_1 = 7.958 \times 10^{-2}$ and $\sigma_{s,d,i} = 0$. The absorptance increases with size parameter due to the increasing bulk extinction coefficient (while keeping n_2/n_1, k_2/k_1 and $\sigma_{d,s,i}$ constant). At these size parameters, with the given value for k_1, the gas phase exhibits opacity ($\beta_{d,1} d_{pore} > 1$). The decomposed carbon phenolic sample, which has the highest porosity of the four samples, shows the strongest absorptance and the high density virgin graphite sample shows the lowest. For values of x below 50, a steep increase in absorptance, the rate of which is proportional to sample porosity, is observed. For $x > 150$, the absorptance attains a local asymptote.

A similar behaviour for the absorptance with respect to the size parameter is observed for $k_1 = 7.958 \times 10^{-5}$ as shown in Fig. 7b. In this case, the gas phase extinction coefficient exhibits semi-transparent behaviour at small size parameters ($x < 500$). At large size parameters, the gas phase exhibits opaque behaviour, resulting in the high porosity carbon phenolic sample exhibiting the highest absorptance. It can be seen that at values of $x > 800$, the curves start to cross over, following the same trends observed for $k_1 = 7.958 \times 10^{-2}$ with the highest absorptance observed for highest porosity decomposed carbon phenolic. These curves are expected to asymptotically attain their local maxima at even higher size parameters.

Table 4
Equilibrium concentrations of phenolic products at 3000 K and 101325 Pa.

Species	C	CO	H_2	C_2H_2	H	C_4H_2	C_2H
Mass fraction (n.d)	5.93×10^{-1}	2.98×10^{-1}	5.51×10^{-2}	4.44×10^{-2}	5.78×10^{-3}	2.21×10^{-3}	1.51×10^{-3}

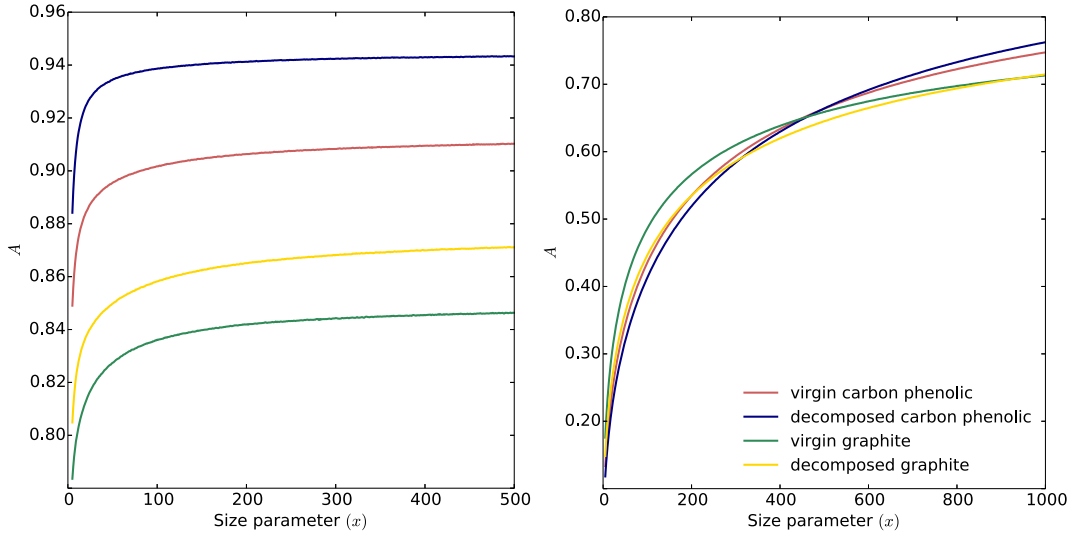

Fig. 7. Absorptance of a 10 mm thick slab composed of the four samples exposed to diffuse irradiation for different size parameters (x_{ref}), for $n_2/n_1 = 2$, $\sigma_{s,d,i} = 0$ and $k_2/k_1 = 0.01$ where (a) $k_1 = 7.958 \times 10^{-2}$ and (b) $k_1 = 7.958 \times 10^{-5}$. (A colour version of this figure can be viewed online.)

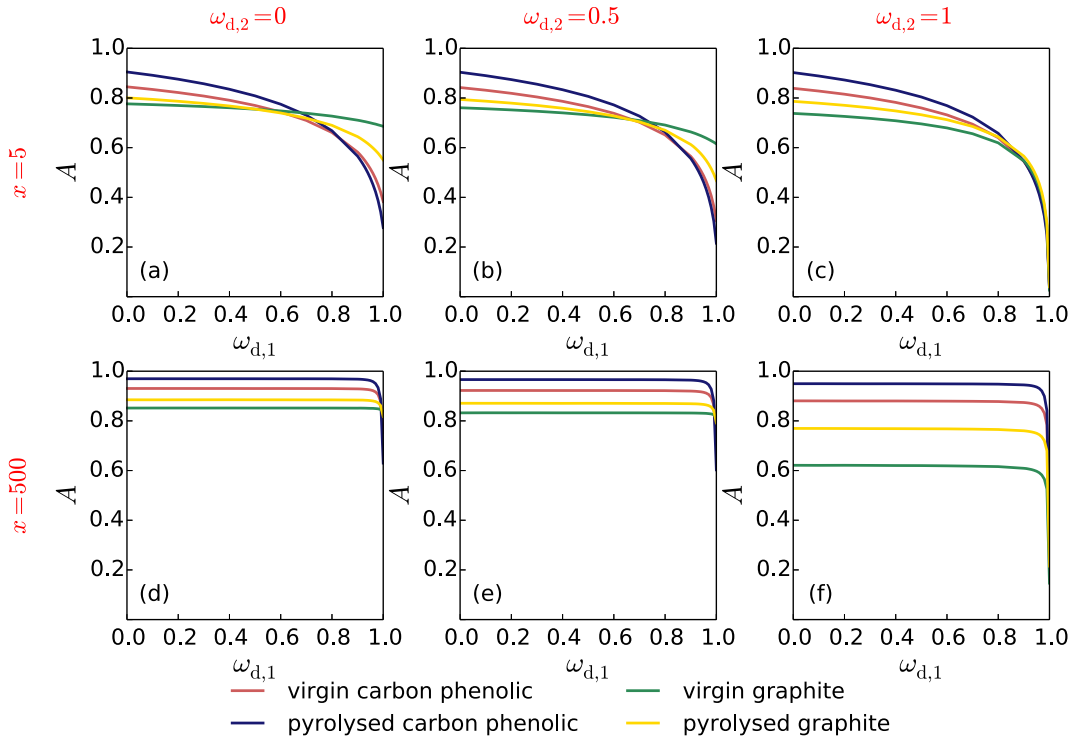

Fig. 8. Absorptance of a 10 mm thick slab exposed to diffuse irradiation. The slab is composed of the four samples for different gas phase scattering albedos ($\omega_{d,1}$) for $k_1 = 7.958 \times 10^{-4}$, $k_2/k_1 = 0.01$ and $n_2/n_1 = 2$. Across - variation of solid phase scattering albedo, $\omega_{d,2} = 0, 0.5, 1$; Down - variation of size parameter, $x = 5$ and 500. (A colour version of this figure can be viewed online.)

At a temperature of approximately 3000 K, the possibility exists for a TPS material's gas phase to attenuate strongly compared to its solid phase. If both phases are strongly absorbing, from Fig. 7a, it can be seen that the decomposed carbon phenolic composite would absorb approximately 88% of the incoming radiation at wavelengths in the near infrared and above ($\lambda \geq 1.25$ μm for $x > 50$). The decomposing graphite reinforced polymer composite would absorb less radiation at 81% due to the less absorbing solid phase making up the majority of its structure.

3.3.4. Scattering effects

The inclusion of scattering, by varying the scattering albedos of both phases, results in a significant change in sample absorptance. Calculated absorptances are plotted in Fig. 8 against gas phase scattering albedos ($\omega_{d,i} = \sigma_{d,s,i}/\beta_{d,i}$). From left to right, the columns present absorptance values calculated by including scattering within the solid phase, by selecting $\omega_{d,2}$ to be equal to 0, 0.5 or 1 with varying $\beta_{d,i}$ for $k_1 = 7.958 \times 10^{-4}$ and $k_2/k_1 = 0.01$. From top to bottom, each row represents a different selected size parameter used in the calculation, $x = 5$ and 500, to demonstrate any wavelength dependency.

For $x = 5$ and $0 \leq \omega_{d,2} \leq 1$ (Fig. 8a, 8b and 8c), a decrease in absorptance for all samples with an increase in $\omega_{d,1}$ is observed. Sample porosity plays an influential role in these results. If the solid volume fraction is high (i.e. virgin graphite), variations in scattering albedo $\omega_{d,1}$ do not significantly affect absorption for $\omega_{d,2} = 0$ and 0.5. This is due to the majority of the sample comprising of the solid phase and thus overall slab reflectance not being significantly augmented by scattering in the gas phase. However, when $\omega_{d,2}$ equals 1, high values of $\omega_{d,1}$ result in a substantial drop in absorptance. Conversely, absorptance in the high porosity decomposed carbon phenolic sample is more significantly affected by increasing $\omega_{d,1}$, and drops even further by increasing $\omega_{d,2}$ due to cumulative scattering effects in both phases.

For $x = 500$ (Fig. 8d, 8e and 8f), discrete extinction coefficients $\beta_{d,i}$ are extremely high and invoke a stronger absorption coefficient $\kappa_{d,i}$ irrespective of the scattering albedos investigated. The absorptance values for each sample therefore remain constant for $0 \leq \omega_{d,1} \leq 0.9$ after which scattering in both phases dominates absorption, leading to a steep increase in reflectance and a corresponding decrease in absorptance.

Carbon fibres used in TPS materials are said to be highly scattering [7], selected to help transfer heat away from the payload via re-radiation. From Fig. 8d, it can be seen that for lower wavelengths ($x = 500$), slab absorptance is mainly based on sample porosity. The percentage of incoming radiation absorbed by the decomposed carbon phenolic sample remains constant at approximately 97% with variations in the solid phase scattering albedo ($\omega_{d,2}$). However, with an increase in scattering, samples with lower porosities begin to reflect more incoming radiation. A large drop in absorptance is thus seen for the decomposing graphite reinforced polymer composite. At higher wavelengths ($x = 5$), shown in Fig. 8a, 8b and 8c, absorption behaviour is affected grately by scattering in the gas phase in addition to the aforementioned variables. For a highly scattering gas phase, the decomposed carbon phenolic sample with the highest porosity reflects the largest amount of incoming radiation. Optimising a TPS for re-radiation behaviour therefore requires a compromise between density (porosity) and spectrally resolved scattering properties dependant on the relevant flight conditions.

The presented results can be used as a library of absorption and scattering data for a macroporous sample and be incorporated into any continuum modelling of chemically reacting media, such as a pyrolysing TPS material, gasifying biomass or oxidising fibres (assuming they have similar morphologies). The individual cells of

the computational domain would have to be checked for the reaction convergence state or the composition of the pyrolysis gas at every time-step after which the radiative characteristics of the cell can be calculated and updated based on the given correlations. For example during atmospheric entry, the increasing reaction front in the TPS material results in time-dependent (decomposition extent), variable optical properties in the TPS through its thickness.

4. Conclusions

Accurate radiative modelling and characterisation of reacting carbonaceous macroporous media consisting of at least two semi-transparent phases is essential for applications in the space, chemical and solar-thermal industries. A multi-scale methodology based on computed tomography and Monte Carlo ray tracing was used to determine the macroscopic optical properties of such samples. More specifically, the aim was to understand above which threshold individual bulk phase properties start to dominate overall absorption behaviour and the dependence of this dominance on sample morphology. Furthermore, the changes in optical properties during the decomposition of the carbonaceous samples were quantified. The analysis was applied to two thermal protection system material samples, a medium density carbon phenolic composite and a high density graphite reinforced polymer composite. The exact 3D morphologies of the materials' complex porous structures were recorded using high resolution synchrotron computed tomography with a spatial resolution of 0.33 μm. Once segmented, direct pore level simulations were used to determine the effective radiative properties, namely, the effective extinction and scattering coefficients and the scattering phase functions.

The volume averaged radiative transfer equations were then used to determine the overall reflectance, absorptance and transmittance of semi-infinite slabs of the TPS materials. The effect of wavelength on these properties was evaluated for a range of size parameters ($5 < x < 1000$) and the effect of scattering in the bulk phases was also evaluated ($0 \leq \omega_{d,1} \leq 1$; $0 \leq \omega_{d,2} \leq 1$). Extent of material decomposition was seen to significantly affect the radiative behaviour of the TPS samples. Absorptance during decomposition increased from 0.76 to 0.94 for carbon phenolic and from 0.82 to 0.84 for graphite. Reflectance decreased from 0.24 to 0.06 and from 0.18 to 0.16 respectively. The increase in absorption was greater for the lower density carbon phenolic compared to the high density graphite reinforced polymer composite.

This is a significant result, especially given the aim of replacing older, denser TPS materials with newer, more porous and lighter ones. Given knowledge of the bulk properties, the data presented can be incorporated in heat transfer calculations of macroporous media applied in the space or solar energy conversion domains, in order to quantify, design and optimise these applications.

Acknowledgements

This work is supported by the Swiss National Science Foundation (SNSF) under contract no. 200021–146710 and the European Space Agency TRP-ARC under contract no. 4000106422/12/NL/AF. The authors would like to acknowledge the Paul Scherrer Institut, Villigen, Switzerland for provision of synchrotron radiation beam time at the TOMCAT beamline of the SLS and Dr. Julie Fife for her assistance.

References

[1] M. Stackpoole, S. Sepka, I. Cozmuta, D. Kontinos, Post-flight evaluation of stardust sample return capsule forebody heatshield material, in: AIAA Paper 1202, 2008 https://arc.aiaa.org/doi/abs/10.2514/6.2008-1202.
[2] J.C. Ferguson, F. Panerai, J. Lachaud, A. Martin, S.C.C. Bailey, N.N. Mansour, Modeling the oxidation of low-density carbon fiber material based on micro-tomography, Carbon 96 (2016) 57–65.
[3] G. Duffa, Ablative Thermal Protection Systems Modeling, American Institute of Aeronautics and Astronautics, 2013.
[4] L. Daryabeigi, G.R. Cunnington, J.R. Knutson, Combined heat transfer in high-porosity high-temperature fibrous insulation: theory and experimental validation, J. Thermophys. Heat Transf. 25 (4) (2011) 536–546.
[5] K. Daryabeigi, G.R. Cunnington, J.R. Knutson, Heat transfer modeling for rigid high-temperature fibrous insulation, J. Thermophys. Heat Transf. 27 (3) (2013) 414–421.
[6] S.C. Lee, Effect of fiber orientation on thermal radiation in fibrous media, Int. J. Heat Mass Transf. 32 (2) (1989) 311–319.
[7] S.C. Lee, S. White, J.A. Grzesik, Effective radiative properties of fibrous composites containing spherical particles, J. Thermophys. Heat Transf. 8 (3) (1994) 400–405.
[8] M. Tancrez, J. Taine, Direct identification of absorption and scattering coefficients and phase function of a porous medium by a monte carlo technique, Int. J. Heat Mass Transf. 47 (2) (2004) 373–383.
[9] F. Bellet, E. Chalopin, F. Fichot, E. Iacona, J. Taine, Rdfi determination of anisotropic and scattering dependent radiative conductivity tensors in porous media: application to rod bundles, Int. J. Heat Mass Transf. 52 (5) (2009) 1544–1551.
[10] S. Le Foll, F. André, A. Delmas, J.M. Bouilly, Y. Aspa, Radiative transfer modelling inside thermal protection system using hybrid homogenization method for a backward Monte Carlo method coupled with Mie theory, J. Phys. Conf. Ser. 369 (1) (2012) 12–28.
[11] J. Petrasch, P. Wyss, A. Steinfeld, Tomography-based Monte Carlo determination of radiative properties of reticulate porous ceramics, J. Quant. Spectrosc. Radiat. Transf. 105 (2) (2007) 180–197.
[12] S. Haussener, W. Lipiński, P. Wyss, A. Steinfeld, Tomography-based analysis of radiative transfer in reacting packed beds undergoing a solid-gas thermochemical transformation, J. Heat Transf. 132 (6) (2010) 061201.
[13] S. Haussener, M. Gergely, M. Schneebeli, A. Steinfeld, Determination of the macroscopic optical properties of snow based on exact morphology and direct pore-level heat transfer modeling, J. Geophys. Res. Earth Surf. 117 (F3) (2012).
[14] W. Lipiński, J. Petrasch, S. Haussener, Application of the spatial averaging theorem to radiative heat transfer in two-phase media, J. Quant. Spectrosc. Radiat. Transf. 111 (1) (2010) 253–258.
[15] W. Lipiński, D. Keene, S. Haussener, J. Petrasch, Continuum radiative heat transfer modeling in media consisting of optically distinct components in the limit of geometrical optics, J. Quant. Spectrosc. Radiat. Transf. 111 (16) (2010) 2474–2480.
[16] J. Petrasch, S. Haussener, W. Lipiński, Discrete vs. continuum-scale simulation of radiative transfer in semitransparent two-phase media, J. Quant. Spectrosc. Radiat. Transf. 112 (9) (2011) 1450–1459.
[17] M. Chahlafi, F. Bellet, F. Fichot, J. Taine, Radiative transfer within non beerian porous media with semitransparent and opaque phases in non equilibrium: application to reflooding of a nuclear reactor, Int. J. Heat Mass Transf. 55 (13) (2012) 3666–3676.
[18] V. Leroy, B. Goyeau, J. Taine, Coupled upscaling approaches for conduction, convection, and radiation in porous media: theoretical developments, Transp. Porous Media 98 (2) (2013) 323–347.
[19] R. Viskanta, M.P. Mengüç, Radiation heat transfer in combustion systems, Prog. Energy Combust. Sci. 13 (2) (1987) 97–160.
[20] J.M. Bouilly, F. Bonnefond, L. Dariol, P. Jullien, F. Leleu, Ablative thermal protection systems for entry in Mars atmosphere. A presentation of materials solutions and testing capabilities, in: The 4th International Planetary Probe Workshop, Pasadena, CA, 2006.
[21] Mersen CALCARB HD, https://www.mersen.com/uploads/tx_mersen/3-CALCARB-rigid-carbon-thermal-insulation-mersen_04.pdf, (Accessed 20 04 2017).
[22] S. Haussener, W. Lipiński, J. Petrasch, P. Wyss, A. Steinfeld, Tomographic characterization of a semitransparent-particle packed bed and determination of its thermal radiative properties, J. Heat Transf. 131 (7) (2009) 072701.
[23] N. Banerji, P. Leyland, S. Haussener, Coupling internal radiation to material response of thermal protection systems, in: 8th European Symposium on Aerothermodynamics for Space Vehicles, Lisbon, Portugal, 2015.
[24] M. Stampanoni, A. Groso, A. Isenegger, G. Mikuljan, Q. Chen, A. Bertrand, S. Henein, R. Betemps, U. Frommherz, P. Böhler, et al., Trends in synchrotron-based tomographic imaging: the sls experience, in: SPIE Optics+ Photonics, International Society for Optics and Photonics, 2006, 63180M–63180M.
[25] J.G. Berryman, S.C. Blair, Use of digital image analysis to estimate fluid permeability of porous materials: application of two-point correlation functions, J. Appl. Phys. 60 (6) (1986) 1930–1938.
[26] Anon, User's Manual, Aerotherm Charring Material Thermal Response and

Ablation Program (CMA87), Tech. Rep. UM-87–11/ATD, Acurex Corporation, Aerotherm Division, Mountain View, CA, 1987.
[27] G.F. Sykes Jr., Decomposition Characteristics of a Char-forming Phenolic Polymer Used for Ablative Composites, Tech. Rep. TN D-3810, NASA, 1967.
[28] G.C. April, R.W. Pike, E.G. Del Valle, Modeling reacting gas flow in the char layer of an ablator, AIAA J. 9 (6) (1971) 1113–1119.
[29] H.J. Vogel, Morphological determination of pore connectivity as a function of pore size using serial sections, Eur. J. Soil Sci. 48 (3) (1997) 365–377.
[30] J.R. Howell, M.P. Mengüç, R. Siegel, Thermal Radiation Heat Transfer, CRC Press, 2010.
[31] C. Tien, B. Drolen, Thermal radiation in part1culate media with dependent and independent scattering, Annu. Rev. Heat Transf. 1 (1) (1987).
[32] S. White, Radiation Testing of PICA at the solar power tower, in: 10th AIAA/ASME Joint Thermophysics and Heat Transfer Conference, vol. 28, 2010. Chicago, IL.
[33] A. Smith, J. Beck, M. Fertig, H. Liebhart, L. Marraffa, Plasma Radiation Database Parade V3. 1, ESA Contract Rept. TR28/96 No 8, 2011. http://adsabs.harvard.edu/full/2003ESASP.533...75S.